Check for updates

Cylindrical illumination with angular coupling for whole-prostate photoacoustic tomography

Brittani Bungart,[1,2,3] **Yingchun Cao,**[3] **Tiffany Yang-Tran,**[4] **Sean Gorsky,**[3] **Lu Lan,**[4] **Darren Roblyer,**[4] **Michael O. Koch,**[6] **Liang Cheng,**[5] **Timothy Masterson,**[6] **and Ji-Xin Cheng**[3,4,*]

[1]*Weldon School of Biomedical Engineering, Purdue University, 206 S. Martin Jischke Drive, West Lafayette, IN 47907, USA*
[2]*Medical Scientist Training Program, Indiana University School of Medicine, 635 Barnhill Drive MS 2031, Indianapolis, IN 46202, USA*
[3]*Department of Electrical and Computer Engineering, Boston University, 8 St. Mary's Street, Boston, MA 02215, USA*
[4]*Department of Biomedical Engineering, Boston University, 44 Cummington Mall, Boston, MA 02215, USA*
[5]*Department of Pathology and Laboratory Medicine, Indiana University School of Medicine, Indianapolis, IN, USA*
[6]*Department of Urology, Indiana University School of Medicine, Indianapolis, IN, USA*
*jxcheng@bu.edu

Abstract: Current diagnosis of prostate cancer relies on histological analysis of tissue samples acquired by biopsy, which could benefit from real-time identification of suspicious lesions. Photoacoustic tomography has the potential to provide real-time targets for prostate biopsy guidance with chemical selectivity, but light delivered from the rectal cavity has been unable to penetrate to the anterior prostate. To overcome this barrier, a urethral device with cylindrical illumination is developed for whole-prostate imaging, and its performance as a function of angular light coupling is evaluated with a prostate-mimicking phantom.

1. Introduction

Prostate cancer is the most incident cancer in men with an estimated 164,690 new cases diagnosed in 2018 [1]. To confirm the presence of prostate cancer after prostate specific antigen screening, initial tissue biopsies are now acquired using the magnetic resonance imaging (MRI) fusion-guided prostate biopsy protocol. For this approach annotated MRI images are overlaid on real-time US imaging to guide sampling of suspicious regions marked by uroradiologists, and additional biopsy samples are acquired via the templated transrectal ultrasound (US)-guided prostate biopsy protocol [2–6]. While this approach improves the sensitivity of the prostate biopsy, a real-time imaging method of identifying suspicious regions to biopsy could help overcome some of the pitfalls of the MRI fusion-guided prostate biopsy [7–9].

Photoacoustic tomography (PAT), a hybrid optical imaging technique, has high clinical translatability due to its increased imaging depth compared to pure optical imaging modalities. The photoacoustic (PA) signal is generated by photon absorption in biological tissue, which is subsequently released as heat. The resulting localized thermoelastic expansion generates an acoustic wave, which can then be detected by traditional clinical US transducer arrays [10–14]. In recent years, PAT has been applied to many clinical topics, such as the neurological system [15–18], breast cancer [19–23], the female reproductive tract [24–26], the gastrointestinal system [27,28], atherosclerosis [29–33], prostate cancer [34–43], the urological system [44–50], melanoma [51–55], and fibrosis [56,57].

PAT can provide real-time imaging for the prostate cancer biopsy since the same US transducers used for the current biopsy protocol can be used to collect the PAT signal. The

combination of PAT and US imaging can then provide spectroscopic and anatomical information [34–40,42,43]. Angiogenesis and lipid accumulation have been shown to be increased in prostate cancer tumors [58,59]. *In vivo* [43] and *ex vivo* [34,35,41] imaging of human prostates have shown differences between malignant and benign prostate tissue using endogenous contrast. We have recently shown that successful prostate cancer biopsy targeting in *ex vivo* human prostates is possible using 1064 nm PAT and US imaging [34].

While PAT has the potential to provide real-time biopsy targets, current PAT setups have not yet demonstrated the ability to image the full posterior-anterior depth as observed from the rectum with the US transducer [34,35,41–43]. Two locations for the placement of the light delivery source for PAT have been investigated. The first location is placing the light delivery mechanism with the US transducer in the rectum. Simulation studies [60] along with *in vivo* [42,43] and *ex vivo* [34] PAT of human prostates have shown that the anterior regions of the prostate do not receive adequate light fluence to detect malignant and benign signal contrast when a rectally-located illumination source is used. The second location, which shows improved potential for PAT of the anterior prostate [60], is to deliver light via the prostatic urethra. A couple of transurethral light delivery designs have been employed for transrectal prostate PAT imaging, including a bevel-tipped fiber [61] and a fiber with a diffuser end [37]. While the recently published transurethral illumination device with diffuser end improved the illumination volume [37], neither of these transurethral light delivery designs has demonstrated the ability to deliver enough light uniformly for whole-prostate illumination, which is ideal since the detector and illumination source are separated.

To illuminate the entire prostate via the prostatic urethra, cylindrical illumination is needed compared to light delivery methods that have limited axial thickness, e.g. bevel-tipped fibers [61]. One reason for needing a cylindrical illumination is that the urologist is manually controlling the US probe during the biopsy procedure [5]. Thus, alignment of the US transducer array's acceptance plane and the region from which the PA signal is generated is difficult unless large volumes of the prostate generate PA signal. In addition, since the patient is awake for the prostate biopsy procedure, any rotation and/or pullback of the illumination device may cause patient discomfort. For these reasons a light delivery source with a cylindrical diffuser is needed.

While cylindrical diffusers have been used for photodynamic therapy for decades [62,63], their application in PAT is just emerging [37,41,64]. The process of fabricating a cylindrical diffuser typically entails methods that use acid etching [37,64] or laser micro-machining with a uniform pattern created on the fiber surface [65]. Using the acid etching method, Ai *et al.* created a 3.0 cm long diffuser on the end of a 1.0 mm core multimode fiber (MMF). A maximum coupling energy of 40 mJ/pulse was demonstrated with two-thirds of the energy converted from forward firing to side firing. To increase the energy fluence to enable deep PAT, a parabolic mirror was incorporated to achieve an estimated 10 mJ/cm^2 energy fluence at the tissue surface. The final diameter of the transurethral light delivery device was 25 French or 8.33 mm, which includes the 1.0 mm core MMF diffuser, parabolic mirror and rigid cystoscope sheath. This design illuminates roughly one-fourth of the axial plane along the whole caudal-to-cranial axis of the prostate, which is an improvement over the bevel-tipped MMF design [61]. Similarly, the laser micro-machining method used to create a diffusing fiber for treatment of urethral stricture demonstrated forward energy leakage from the end of the diffuser end, while the majority of the energy was converted to side firing [65]. Most recently, Li *et al.* demonstrated the ability to detect PA signal generated 1 cm from a cylindrically-diffusing MMF end made with acid etching. While the forward propagation to side firing energy conversion was not evaluated, this study shows that deep PAT imaging is possible using a cylindrically diffusing fiber end. Based on this prior literature, the efficient conversion of forward to side firing energy in cylindrically diffusing MMFs needs to be improved to enable illumination of the whole prostate for PAT.

A commonly used approach to couple photons into a fiber is through a collinear geometry. Instead, we found that deviating the coupling from the collinear geometry significantly improves the conversion of forward propagation to side illumination, while not reducing the light-fiber coupling efficiency. Based on this counterintuitive finding, we developed a simple and efficient method of cylindrical illumination by sandpaper machining of a MMF end and angular coupling of light into the MMF. After characterization of the angular coupling effect on the emission profiles, we demonstrate the potential of our device for whole-prostate PAT by volumetric imaging of a prostate-mimicking tissue phantom with a single laser shot.

2. Methods

2.1 PAT setup with angularly-coupled transurethral light delivery

For this study a 1064 nm PAT device with transrectal US and transurethral light delivery was employed (Fig. 1). This 1064 nm PAT imaging setup is similar to our previously published work [34] with a few minor changes. A highly compact, 6 W Nd:YAG laser with 8 ns pulse width (CFR300, Quantel-USA, Bozeman, MT, USA) was incorporated with our US system (Verasonics, Kirkland, WA, USA). The laser's 10 Hz repetition rate was externally controlled, and the laser's beam diameter was 12 mm. A Galilean beam reducer was installed before MMF coupling to achieve a 2 mm beam diameter to approximately match the diameter of the MMF's core. A C9-5ICT transrectal US transducer (Philips, Andover, MA, USA) was used for US imaging and collection of the PA signal.
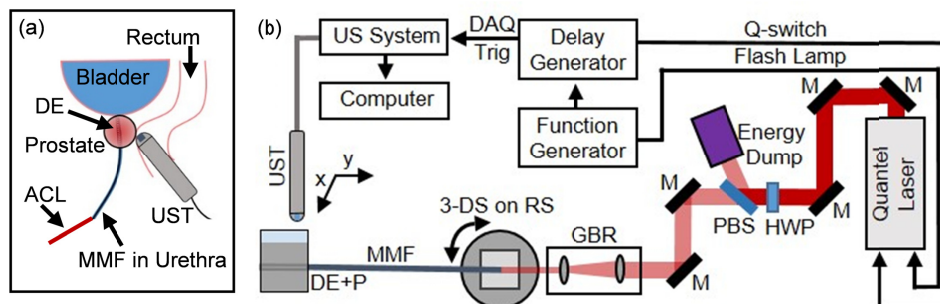

Fig. 1. PA and US tomography with angularly-coupled transurethral light delivery setup. (a) Transurethral light delivery with transrectal US imaging and PA signal collection is depicted. (b) A schematic is shown of the PA and US tomography setup used for this study. DE: diffuser end; ACL: angularly-coupled light; MMF: multimode fiber; UST: ultrasound transducer; DAQ Trig: data acquisition system trigger; M: Nd:YAG laser line 45° mirror; HWP: half wave plate; PBS: polarized beam splitter; GBR: Galilean beam reducer; 3-DS on RS: 3-dimensional stage on rotational stage; DE + P: diffuser end + phantom.

2.2 Cylindrically-diffusing fiber fabrication

To test a sandpaper abrasion method for creating a MMF diffuser, the ends of a 1.5 mm diameter core MMF (FP1500ERT, Thorlabs, Newton, NJ, USA) were cleaved and polished using a NanoPol Polisher (Ultra Tec Manufacturing, Inc., Santa Ana, CA, USA) with 30 μm to 0.02 μm grit diamond lapping sheets (Thorlabs, Newton, NJ, USA). The jacket and cladding were removed from the fiber's end with a razor blade (Fig. 2(a)), which was the last 3.0 cm of the 1.5 mm core MMF for the initial test. Following removal of the jacket and cladding, the proximal 1.0 cm of the MMF's bare core was abraded in a multidirectional manner using a 30 μm grit fiber polishing sheet (LF30D, Thorlabs, Newton, NJ) until the abrasion appeared uniform under 10X magnification and no smooth regions of glass were observed (Fig. 2(c)). 30 μm grit size was chosen since 30 μm is similar to the groove width for a previously published laser micro-machined fiber diffuser [65]. To qualitatively observe the light diffusion, 405 nm was coupled to the fiber (Fig. 2(c)).

For the final diffusing fiber design, a 2.0 mm core MMF (APC2000, Fiberguide Industries, Stirling, NJ) with a numerical aperture of 0.37 was used to create a 60 cm fiber with a 5.0 cm diffuser end. Similarly, the ends of the fiber were cleaved and polished. The jacket and cladding were then removed with a razor blade (Fig. 2(a)). The diffuser was then fabricated using 320 grit sandpaper (Miady, Amazon) to abrade only the side of the bare fiber end (Fig. 2(b)). The fiber was sanded in a multidirectional manner until it appeared uniform under 10X magnification with no smooth glass apparent. The end surface of the diffuser was kept polished to measure forward-leaking energy.
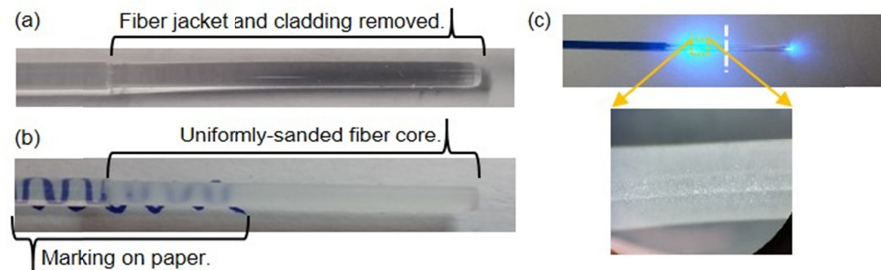

Fig. 2. Fabrication of fiber with sandpaper-abraded diffuser end. (a) The jacket and cladding are removed from the end of a 2 mm core multimode fiber. (b) The fiber core's surface underwent abrasion with sandpaper. A blue sine wave is drawn on the paper behind part of the abraded and unabraded fiber. (c) Light diffusion is shown at the end of a 1.5 mm core multimode fiber with abrasion from sandpaper located left of the white dashed line. The surface of the sandpaper-abraded fiber core (orange box) is shown under 10X magnification.

2.3 Measurement of fiber coupling and side firing efficiency

Energy measurements were acquired using a 1064 nm calibrated energy sensor (QE25SP-S-MT-D0, Gentec-EO, Lake Oswego, OR, USA) in combination with the Maestro console (Gentec-EO, Lake Oswego, OR, USA), which can connect to a computer for data acquisition. The MMF was mounted using a large core fiber holder (HFS001, Thorlabs, Newton, NJ, USA) that was clamped to a 3-dimensional stage (MBT621D, Thorlabs, Stirling, NJ, USA). This setup was then mounted onto a manual rotational stage (RP03, Thorlabs, Stirling, NJ, USA) such that the coupling from 0° to the maximum coupling angle of the fiber, which was 21.7° based on the numerical aperture, could be tested.

Fiber coupling stability when removing and reinstalling a MMF was determined by measuring the pulse energy before and after a non-diffusing MMF with polished, cleaved ends. A non-diffusing MMF was used as it is difficult to ensure all energy is measured from the diffuser end. An iris was mounted on the energy sensor so that 1064 nm energy not propagating out the fiber end could be blocked from the sensor. Between each set of measurements from 5° to 20°, the fiber was removed from the fiber holder and placed back in the fiber holder without realignment, i.e. repositioning of the multidirectional stage. Three sets of measurements were collected of 50 pulses per coupling angle. The average and standard deviation of the 3 measurements were plotted.

After determining that fiber coupling was stable when switching fibers, the percentage of energy converted to side firing emission was studied by initially measuring the coupling efficiency of a non-diffusing MMF as described in the previous paragraph. Coupling angles from 0° to beyond the MMF's maximum acceptance angle were used. A MMF with a diffusing end then replaced the non-diffusing MMF in the optical pathway. The forward firing energy from the diffuser end was measured with an iris used to block the side-fired energy from the diffuser end. A total of 50 pulses were measured and averaged for each data point and plotted with the error bars representing the standard deviation of the data points.

2.4 Emission profile measurement of fiber diffuser end

The same Gentec-EO energy sensor and console were used for all energy measurements to determine emission profiles. A 1 mm wide slit was created using razor blades. This slit was then attached to the energy sensor, which resulted in 1 mm by 25 mm slit, with the slit's long axis parallel to the MMF's long axis. The sensor with slit was mounted to a motorized rotational stage (PRM1Z8, Thorlabs, Newton, NJ, USA), which was then attached to two overlapping 25 mm 1-dimensional stages (423 Series, Newport Corporation, Irvine, CA, USA). The MMF's diffuser end was positioned so that the energy sensor would be equidistant during all measurements. The radial emission profile was measured every 15°. To measure the longitudinal emission profile, the slit was rotated 90° and oriented perpendicular to the MMF's long axis. The longitudinal emission was measured every 2 mm along the diffuser end. The plotted data is the average of 50 pulses.

2.5 Determining energy fluence at the capillary tube-tissue interface

First, the stability of the diffuser end's longitudinal emission profiles was determined when the coupling energy changed. The pulse energy was modulated with neutral density (ND) filters (Thorlabs, Newton, NJ, USA), and then, the longitudinal emission profiles were measured as described above. The curves with ND filters applied were divided by the non-filtered emission curves. These normalized curves should have little to no slope if the longitudinal emission profile does not change with pulse energy coupled. Also, the y-intercept should approximate the 1064 nm transmission data from the ND filters product information.

After confirming the longitudinal emission profile stability when changing energy coupled into the MMF, the maximum coupled energy per pulse was determined to conform to the ANSI guidelines for tissue damage threshold, which is 100 mJ/cm^2/pulse for 1064 nm and our laser's pulse characteristics [66]. To do this the area under the curve (AUC) was calculated from the diffuser end's longitudinal emission curves. Each longitudinal emission profile was normalized by its own maximum energy so that the normalized peak energy equaled 1 for each longitudinal emission profile. The x-axis of the normalized longitudinal emission profiles was divided by 5 cm, so that the resulting AUC values would range from 0 to 1. Then, a uniform longitudinal emission profile with an AUC value of 1 was initially assumed. For a maximum energy fluence of 100 mJ/pulse/cm^2, the coupled pulse energy was then calculated to be 628.3 mJ/pulse based on a glass-capped diffuser end with 2 mm radius and 50 mm length. Then, this value was divided by the ratio of side-fired energy to total energy coupled for each coupling angle to account for energy emitting from the tip of the diffuser end. These values were then multiplied by the AUC values for the normalized longitudinal emission profiles.

2.6 Prostate tissue-mimicking phantom design, validation and fabrication

To create a PA prostate tissue-mimicking phantom, the optical and acoustic properties need to be considered. For human prostate tissue, the optical properties at 1064 nm are 0.78 cm^{-1} for the absorption coefficient and 6.3 cm^{-1} for the reduced scattering coefficient [67]. For the acoustic properties, the speed of sound in human prostates is 1529 m/s, while the attenuation coefficient and slope at 5.0 MHz is 2.35 dB/cm and 0.72 dB/cm/MHz [68]. Based on these properties, 8% type A, 300-Bloom porcine gelatin (G2500, Sigma-Aldrich, St. Louis, MO, USA) was chosen for its similar acoustic properties, while being optically transparent [69,70]. To modify the optical properties of the phantom, Intralipid fat emulsion solution and black India ink have been well studied for tuning the optical properties of tissue-mimicking phantoms [69,71].

To determine the concentration of black India ink and Intralipid-20% fat emulsion solution to achieve optical properties similar to human prostate tissue, a spectrophotometer (DU 530, Beckman Coulter, Brea, CA, USA) was used to measure 1064 nm transmittance

through phantom components. Three independent measurements per phantom component concentration were collected. The sample volume loaded into the cuvette (14-955-129, Fisher Scientific, Hampton, NH, USA) was 300 µL and was kept constant over all measurements to minimize error. An air-filled cuvette was used as a blank reference to obtain a measurement value for ultrapure water to compare to literature. To correct for reflection differences between an air- and a water-filled cuvette, the Fresnel equations were employed with the light's angle of incidence perpendicular to the interfaces [72]. The refractive indexes used were 1.00, 1.51, and 1.33 for air, the cuvette [73], and water respectively. The ratio of the theoretical transmission through an air-filled cuvette to a water-filled cuvette was calculated to be 0.92, which was then multiplied to the transmission data to correct for the reflection differences. The corrected transmission data was then used to calculate the reduced optical extinction coefficient (μ_t') as

$$\mu_t' = \frac{1}{z}\ln[l] \qquad (1)$$

where z is the path length through the cuvette in cm and I is the corrected fraction of light intensity transmitted through sample over light intensity transmitted through air in a 1 cm cuvette [69]. This calculation is valid for a diluted highly scattering media if the inverse of the reduced optical extinction coefficient is equal to or less than the sample length [69,74].

For the concentrations of black India ink and Intralipid-20% fat emulsion solution that give optical properties similar to human tissue, the reduced optical extinction coefficient, which is a summation of the reduced scattering (μ_s') and the absorption coefficient (μ_a), reduces to the absorption coefficient for black India ink's values and primarily to the reduced scattering coefficient for Intralipid-20% fat emulsion solution's values [71]. Therefore, the optical extinction coefficient values for black India ink were plotted as absorption coefficient over concentration. For Intralipid-20% fat emulsion solution, the optical extinction coefficient value of water was subtracted from the data since this value is primarily comprised of absorption. The resulting values that had a mean free path less or equal to 1 cm, were then plotted as the reduced scattering coefficient over concentration. The linear fitting of these two plots were used to calculate the phantom components' concentration to achieve optical properties that approximate human prostate tissue's optical properties.

The mold for the prostate phantom comprised of a 5 cm by 11 cm plastic container with 7 cm depth (Ziploc medium rectangle, S. C. Johnson & Son, Racine, WI, USA). Holes were drilled into the sides of the container for the 4 mm outer diameter glass capillary tube (246 040 080, Friedrich & Dimmock, Inc., Millville, NJ, USA) and 0.5 mm pencil leads, which were placed 1.5 cm from the surface of the capillary tube. After insertion of the capillary tube and pencil leads, epoxy was used to create a waterproof seal. The phantom mixture was prepared as previously described [69]. Then, the mixture was poured into the mold and allowed to incubate overnight in 4°C before imaging. The phantom was used within 3 days to ensure stability.

3. Results

3.1 Angular coupling enhances forward propagation to side emission conversion efficiency

After aligning the coupling plane of the MMF to the axis of the rotational stage, the coupling stability when removing and reinstalling a MMF was confirmed to be stable between independent measurements without adjusting the stage position (Fig. 3(a)). The coupling efficiency between each installment of the MMF on the holder was consistent as the standard deviation was at most 1.1% for coupling angles from 5° to 20°. The coupling efficiency was then examined for coupling angles that covered all of the MMF's acceptance angles, which is from 0° to 21.7° (Fig. 3(b)). The coupling efficiency is between 73.6% and 81.7% for the

angles up to the maximum acceptance angle. After a coupling angle of 22°, the coupling efficiency drops to 38.8%.

The efficiency of the coupled light to emit from the side of the diffuser end as opposed to leaking out the end is shown in Fig. 3(c). When the coupling angle is 0°, the majority of energy per pulse is observed to emit from the MMF end with only 25.7% of the energy emitting from the diffuser's side. The conversion to side firing steeply improves to 92.8% as the coupling angle is increased to 8°. Then, the side firing conversion efficiency gradually increases to 98.8% by the maximum accepting angle of the MMF.
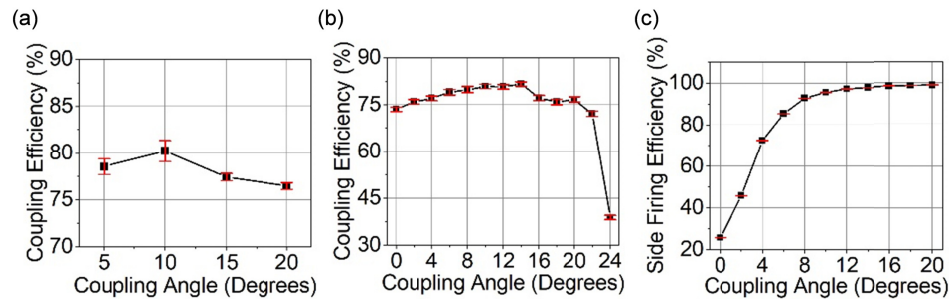

Fig. 3. Coupling angle affects side emission conversion efficiency of the diffuser-ended fiber. (a) Fiber coupling efficiency at increasing coupling angles when removing and reinstalling fiber to holder. (b) Fiber coupling efficiency shown from 0° coupling angle to past the numerical aperture of the MMF. (c) The percent of energy fired cylindrically from the fiber's diffuser end while increasing the coupling angle of the light.

3.2 Peak in longitudinal emission profile can be shifted by varying the coupling angle

Since the side firing conversion efficiency for the MMF's diffuser end is affected by coupling angle, the emission profiles were also evaluated. To measure the radial emission profile from the MMF's diffuser end, the slit was oriented parallel to the MMF's long axis (Fig. 4(a)), while the slit was oriented perpendicular to the MMF's long axis to characterize the longitudinal emission profiles (Fig. 4(c)). The radial profile is shown to be uniform, but the relative energy is affected by the coupling angle (Fig. 4(b)). The normalized energy for the 0° coupling angle's radial profile ranged from 0.10 to 0.13, while the 10° and 20° have normalized energy ranges of 0.74 to 0.97 and 0.88 to 1.0 respectively. In contrast to the radial emission profile, the longitudinal emission profile does not have the same shape over the coupling angles tested (Fig. 4(d)). The longitudinal emission profiles contain a peak, which shifts from the distal to proximal end of the MMF's diffuser end as the coupling angle is increased. The broadness of the peak also shortens when the coupling angle is increased.

3.3 Longitudinal emission profiles can be used to determine the maximum acceptable coupling energy

Longitudinal emission profiles collected with 10° and 20° coupling angles are constant when ND filters were applied to attenuate the coupled pulse energy (Figs. 5(a) and 5(b)). With the known longitudinal emission profiles and the relatively uniform radial emission profiles, the energy fluence at the capillary tube-tissue interface can be estimated if the longitudinal emission profiles are stable when the pulse energy is modified, which is the case here. The AUC values for the normalized longitudinal emission profiles are shown in Fig. 5(c). The AUC decreases as the coupling angle increases, which equates to a sharpening of the peak found in the longitudinal emission profile. The maximum coupled pulse energy based on the ANSI guidelines [66] when the AUC is 1 for the diffuser-ended MMF here was calculated to be 628.3 mJ/pulse, which was then multiplied by the AUC for each coupling angle. The resulting coupled energy per pulse is the theoretical maximum at which the tissue damage threshold will be reached at each coupling angle (Fig. 5(d)). The maximum coupled pulse

energy ranges from 320 mJ/pulse when using a coupling angle of 20° up to 476 mJ/pulse when an 8° coupling angle is used.
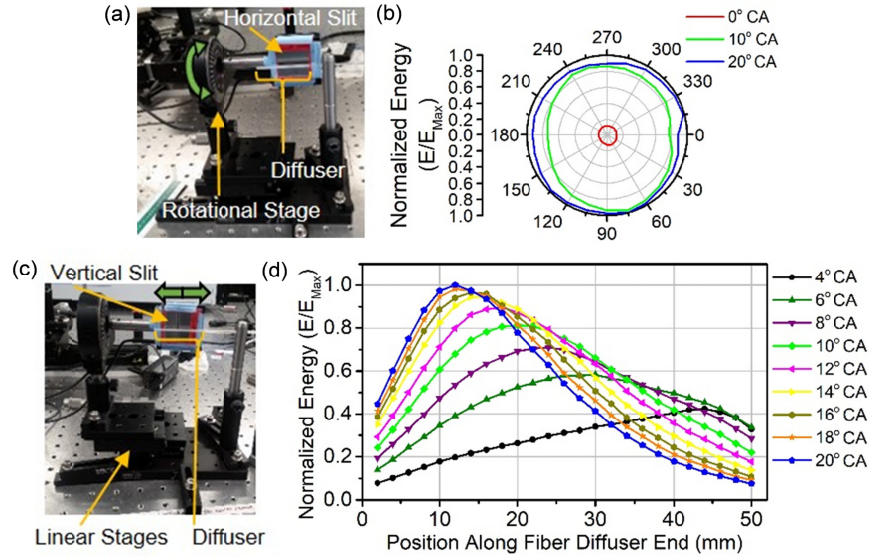

Fig. 4. Diffuser's longitudinal emission profile is controlled by coupling angle. (a) Photograph of sensor with horizontal slit mounted on a rotational stage for radial emission profile data collection. (b) Radial emission profiles with 0°, 10°, and 20° coupling angles were normalized by the maximum energy (E_{Max}) and plotted. (c) Photograph of sensor with vertical slit mounted on a linear stages for longitudinal emission profile data collection. (d) Longitudinal emission profiles with angular coupling from 0° to 20° were normalized by the maximum energy (E_{Max}). CA: coupling angle.
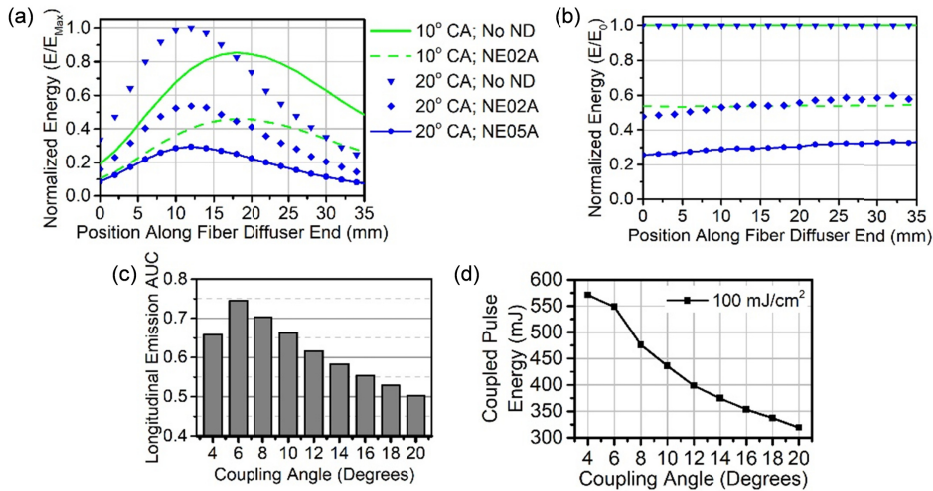

Fig. 5. Longitudinal emission profiles can be used to determine maximum coupling energy based on the tissue damage threshold. (a) Longitudinal emission profiles for 10° and 20° with and without energy attenuation by ND filters are plotted. The profiles are normalized by the maximum energy (E_{Max}). Figure legend also applies to b. (b) The longitudinal emission profiles were also normalized by the profile without a ND filter (E_0). (c) AUC values for longitudinal emission profiles are illustrated over increasing coupling angle. (d) Based on the AUC and the side conversion efficiency at increasing coupling angles, the maximum coupling energy is shown based on 100 mJ/cm²/pulse maximum fluence rate. CA: coupling angle; ND: neutral density filter; NE02A: 0.2 ND filter; NE05A: 0.5 ND filter. AUC: area under the curve.
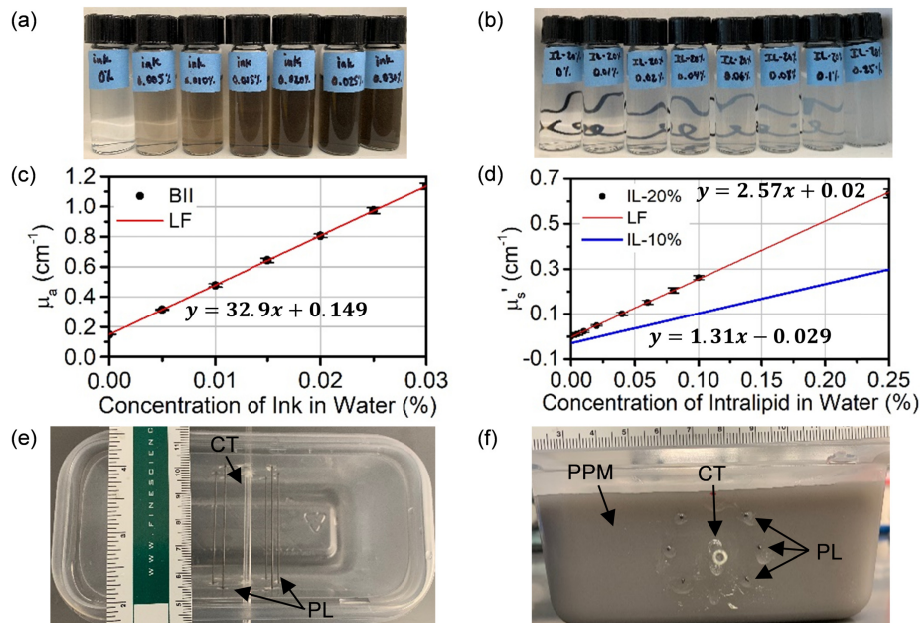
Fig. 6. Controlling the concentration of tissue-mimicking phantom components enables direct, independent tuning of absorption and scattering for single wavelength PAT device testing. (a) Black India ink and (b) Intralipid-20% fat emulsion dilutions are shown that were used to determine μ_a and μ_s' respectively. The background for the ink dilutions is white, while the fat emulsion dilutions' background is white with curved black lines. (c) The calculated μ_a from the black India ink's corrected transmission data is plotted over concentration with a linear-fitted curve. (d) Similarly, a linear curve was fitted of Intralipid-20% fat emulsion's μ_s' over concentration. For comparison the linear fit of Intralipid-10% fat emulsion's μ_s' over concentration from Royston, Poston, and Prahl is plotted. (e) Top-down view of the phantom mold with capillary tube and pencil lead targets epoxied into place. (f) Front view of phantom mold with prostate tissue-mimicking mixture added. BII: black India ink; LF: linear fit curve; IL-20%: Intralipid-20%; IL-10%: Intralipid-10%; CT: capillary tube; PL: pencil lead; PPM: prostate phantom mixture.

3.4 Prostate tissue-mimicking phantom for testing the 1064 nm PAT illumination device

To confirm the radial and longitudinal PA signal generated from the cylindrically-diffusing fiber, a prostate tissue-mimicking phantom with optical properties tuned for 1064 nm PAT needed to be determined. Black India ink and Intralipid-20% emulsion solution are known to primarily tune the absorption and reduced scattering coefficient independently at 1064 nm [71]. Here, we confirm the change in optical coefficients over varying concentration of each component (Figs. 6(a) and 6(b)) for tuning the phantom's optical properties. The linear fit of the black India ink's absorption coefficient (Fig. 6(c)) resulted in a slope of 32.9 cm^{-1}/% and y-intercept of 0.149 cm^{-1}. This linear fit can be used to determine the concentration of black India ink needed for the prostate tissue-mimicking phantom to have an absorption coefficient that approximates human prostate tissue, which is 0.78 cm^{-1} [67]. After subtracting the value of water's absorption coefficient from Intralipid-20% fat emulsion solution's optical extinction coefficient at each concentration, the data was fit with a linear curve for the reduced scattering coefficient (Fig. 6(d)). The slope is 2.57 cm^{-1}/% while the y-intercept is 0.02 cm^{-1}, which can be used to control the phantom's reduced scattering coefficient to approximate human prostate (e.g. 6.3 cm^{-1}). Based on this data, the Intralipid-20% fat emulsion solution's final concentration in the phantom is 2.44%. At this concentration of Intralipid-20% fat emulsion solution some absorption is present. The contribution to the

absorption coefficient is 0.054 cm^{-1}/% for Intralipid-10% fat emulsion solution [71]. After accounting for the 2.44% of the Intralipid-20% fat emulsion solution and water's contribution to the absorption coefficient, the final concentration for black India ink in the phantom is 0.011%. After the pencil lead targets and capillary tube were epoxied into the plastic mold (Fig. 6(e)), the prostate tissue-mimicking phantom was prepared with 8% gelatin and poured into the mold to incubate overnight (Fig. 6(f)).

3.5 PA signal is generated from pencil leads in a prostate tissue-mimicking phantom over the length of the fiber's diffuser end

The prostate tissue-mimicking phantom was allowed to warm to room temperature directly before imaging. The phantom was placed on a sample stage as shown in Fig. 1(b). The diffusing end of the transurethral MMF was inserted in the capillary tube until all 5 cm of the diffuser end was centered in the 5 cm long phantom. Collimated light was coupled into the MMF at 10° and then 20°. Maximum coupled energy into the MMF was approximately 50 mJ/pulse. PAT and US imaging of the prostate tissue-mimicking phantom was performed from the "posterior" side of the phantom in scanning mode with a 0.2 mm step size between imaging frames (Fig. 7(a)). Five imaging scans were completed per fiber coupling angle. No frame averaging was performed. Average peak signal-to-noise ratio (pSNR) of the pencil lead was measured and plotted with error bars representing standard deviation.
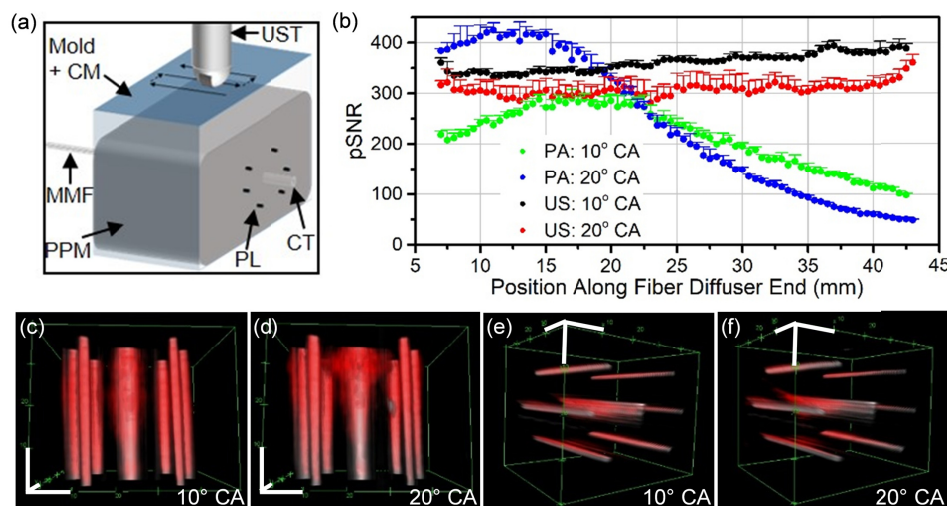

Fig. 7. PA and US signal generated over the prostate tissue-mimicking phantom without moving the illumination source. (a) Schematic shown of experiment. (b) PA and US pSNR from pencil lead targets embedded in prostate tissue-mimicking phantom is graphed over the position along the fiber diffuser from the proximal to distal end. (c-f) Snapshots of 3-dimensional composites comprised of both the US channel (gray) and PAT channel (red) are displayed with 1 cm axis scale bars (white). Snapshots in c and d subpanels have a top-down view, while e and f subpanels' view is of signal from the distal to proximal end of the diffuser. The dynamic range is consistent between all subpanels. The US channel of the composites is in arbitrary units converted to log scale with a range from 10.02 to 14.70, and the PAT channel of the composites is in arbitrary units in the linear scale with a range from 5,397 to 76,920. CM: coupling medium; UST: ultrasound transducer; MMF: multimode fiber; PPM: prostate phantom mixture; PL: pencil lead; CT: capillary tube; CA: coupling angle.

The prostate tissue-mimicking phantom with pencil lead targets underwent 1064 nm PAT and US imaging as depicted in Fig. 7(a). For US and PAT pSNR, the signal is radially-uniform as demonstrated by the error bars representing the standard deviation (Fig. 7b). The pencil leads' US pSNR is relatively constant over the length of the diffuser end, while the PAT pSNR is affected by the coupling angle. The PAT pSNR of the pencil lead is strongest

for the 20° coupling angle, which correlates to the longitudinal emission profile (Fig. 4(d)). While the 10° coupling angle yields a maximum PAT pSNR that is approximately 25% lower than the maximum PAT pSNR for the 20° coupling angle, the peak is broader for the 10° coupling angle, allowing PAT signal to be more uniform over the length of the pencil leads. The 3-dimensional renderings of the PAT and US scans demonstrate the PA signal coinciding with the US signal from the pencil lead (Figs. 7(c)-7(f)). The PAT signal around the capillary tube is generated from the prostate tissue-mimicking phantom.

4. Discussion

4.1 Design of the transurethral illumination source and light coupling method

The cylindrically-diffusing fiber end designed here was inspired by a laser micro-machined design [65]. The benefits of sandpaper abrasion compared to laser micro-machining are that the sensitive alignment of a laser is not needed, and the only equipment needed to make the diffuser fiber here is sandpaper. This fabrication method is also safer and faster compared to the use of etching agent for abrading the surface or creating tapered fiber ends [37,64].

With regard to performance, the sandpaper-abraded fiber diffuser presented here has a radially-uniform emission profile similar to the laser micro-machined fiber diffuser [65]. Additionally, the radial emission profiles of the acid-etched fiber diffusers qualitatively appear uniform, while the longitudinal emission profiles also appear to have a peak [37,64]. Based on these results, our cylindrically-diffusing MMF design has a similar performance regarding the emission profile at a low coupling angle. After considering ray optics, the improved forward to side propagation of light when the coupling angle is increased can be explained by a higher percentage of light interacting with the core surface at the diffuser end [75]. Therefore, we expect other cylindrically-diffusing MMF designs to have an improved forward propagating to side firing energy conversion when the coupling angle is increased. For example, incorporating angular coupling into Ai *et al.*'s transurethral illumination device could allow for reduction of the device's diameter from 8.33 mm to 4 mm. This diameter reduction would reduce the acoustic shadowing of the anterior prostate.

A pitfall to this current study is the rigidity of the MMF, which has a minimum short-term bending radius of 200 mm and minimum long-term bending radius of 400 mm. A more flexible fiber would be ideal, but does not limit clinical translation as rigid urological instrumentation with diameters up to 27 French or 9 mm are commonly inserted into the prostatic urethra [76]. The 2 mm diameter core MMF was chosen to allow for more energy per pulse to be delivered to the prostate phantom as up to 476 mJ/pulse can be delivered by our transurethral illumination source before tissue damage occurs when an 8° coupling angle is used. Besides increasing MMF's core diameter, other methods exist to increase the pulse energy before fiber damage occurs. One method is to optimize the fiber end polishing method and incorporate "front face conditioning" [77]. Another method to reduce damage to the MMF is to reduce the "hot spots" in the spatial profile of the laser beam, which can be done using a beam homogenizer, which must be carefully aligned and designed to minimize diffraction effects [78], or by adjusting the laser's internal alignment [79]. Lastly, the coupled energy can be increased by reducing the peak energy per pulse by using a laser with a longer pulse width, which can range from a few ns to 10s of ns for PA signal generation [80].

If a less rigid MMF is used with the angular coupling approach presented here, increased fiber bending may result in energy loss [75]. During the experiments in this study, fiber bending at or above the minimum long-term bending radius was present. No loss in coupled energy was observed, but the effect of fiber bending on the coupling energy and illumination profiles was not studied. Energy loss can be expected when higher coupling angles that approach the numerical aperture of the MMF and fiber bending are present [75]. If fiber bending results in energy loss, a couple approaches can be taken to minimize the energy loss. One method is to choose the minimum coupling angle that maximizes the forward propagating to side firing conversion of energy at the diffuser end. Here, we show that a 10°

coupling angle, which is 11.7° lower than the MMF's maximum acceptance angle, fulfills the energy conversion requirement while providing longitudinal emission across the length of the fiber for prostate PAT. Another method to overcome the loss of energy due to fiber bending would be to choose a fiber with a higher numerical aperture, which equates to a larger angle to achieve total internal reflection for energy propagation within the MMF [75]. Large core MMFs with higher numerical apertures of are available, such as the 1.5 mm diameter core MMF with 0.5 numerical aperture available via Thorlabs, Inc. (PN: FP1500ERT).

Another pitfall to the illumination design presented here is inherent to cylindrical transurethral light delivery. As the light penetrates the tissue in the radial direction from the diffuser end, the effective surface area increases. Therefore, the energy fluence attenuates over depth due to absorption and this increase in surface area. The maximum possible energy should be used to overcome this pitfall.

4.2 Broader applications of the angle-coupled transurethral light diffuser

The coupling angle-modulated cylindrical light diffuser presented here is optimized for transurethral light delivery for whole-prostate PAT. While this device was developed for use during the prostate biopsy procedure, another prostate-specific application could be intra-operative PAT with da Vinci robotics [81]. Beyond illumination of the prostate for PAT, the light delivery device could be used or altered for other minimally-invasive applications. For instance, this MMF diffuser could be used for PAT of lower gastrointestinal diseases in animal models [57]. This MMF diffuser could also be applied for therapeutic purposes, such as antibiotic re-sensitization of bacteria with phototherapy in urinary tract infections [82].

5. Conclusions

We developed a transurethral light delivery approach for whole-prostate illumination with sandpaper micro-machining of a MMF end. By controlling the coupling angle into the fiber, the energy is efficiently converted and distributed along the length of the diffuser end. The device is kept to an outer diameter of 4 mm, which minimizes anterior prostate acoustic shadowing. The whole-prostate illumination could potentially allow a urologist to freely move the US transducer to identify biopsy targets with PAT and US imaging while the illumination device is statically kept in place.

Funding

Disclosures

The authors declare that there are no conflicts of interest related to this article.

References

1. R. L. Siegel, K. D. Miller, and A. Jemal, "Cancer statistics, 2018," CA Cancer J. Clin. **68**(1), 7–30 (2018).
2. H. U. Ahmed, A. El-Shater Bosaily, L. C. Brown, R. Gabe, R. Kaplan, M. K. Parmar, Y. Collaco-Moraes, K. Ward, R. G. Hindley, A. Freeman, A. P. Kirkham, R. Oldroyd, C. Parker, and M. Emberton; PROMIS study group, "Diagnostic accuracy of multi-parametric MRI and TRUS biopsy in prostate cancer (PROMIS): a paired validating confirmatory study," Lancet **389**(10071), 815–822 (2017).
3. A. Postema, M. Mischi, J. de la Rosette, and H. Wijkstra, "Multiparametric ultrasound in the detection of prostate cancer: a systematic review," World J. Urol. **33**(11), 1651–1659 (2015).
4. Y. Ueno, T. Tamada, V. Bist, C. Reinhold, H. Miyake, U. Tanaka, K. Kitajima, K. Sugimura, and S. Takahashi, "Multiparametric magnetic resonance imaging: Current role in prostate cancer management," Int. J. Urol. **23**(7), 550–557 (2016).
5. M. A. Bjurlin, H. B. Carter, P. Schellhammer, M. S. Cookson, L. G. Gomella, D. Troyer, T. M. Wheeler, S. Schlossberg, D. F. Penson, and S. S. Taneja, "Optimization of initial prostate biopsy in clinical practice: sampling, labeling and specimen processing," J. Urol. **189**(6), 2039–2046 (2013).
6. J. C. Weinreb, J. O. Barentsz, P. L. Choyke, F. Cornud, M. A. Haider, K. J. Macura, D. Margolis, M. D. Schnall, F. Shtern, C. M. Tempany, H. C. Thoeny, and S. Verma, "PI-RADS prostate imaging - reporting and data system: 2015, version 2," Eur. Urol. **69**(1), 16–40 (2016).

7. C. P. Filson, S. Natarajan, D. J. A. Margolis, J. Huang, P. Lieu, F. J. Dorey, R. E. Reiter, and L. S. Marks, "Prostate cancer detection with magnetic resonance-ultrasound fusion biopsy: The role of systematic and targeted biopsies," Cancer **122**(6), 884–892 (2016).

8. M. Davuluri, A. Toler, A. Wojtowycz, G. Bratslavsky, and S. Vourganti, "Cost of prostate MRI-US fusion– a decision analysis comparing cost effectiveness of systematic transrectal ultrasound guided biopsy and MRI-ultrasound Fusion prostate biopsy in the initial and repeat biopsy setting," J. Urol. **193**(4s), e898–e899 (2015).

9. M. A. Perazella, "Gadolinium-contrast toxicity in patients with kidney disease: nephrotoxicity and nephrogenic systemic fibrosis," Curr. Drug Saf. **3**(1), 67–75 (2008).

10. L. V. Wang and J. Yao, "A practical guide to photoacoustic tomography in the life sciences," Nat. Methods **13**(8), 627–638 (2016).

11. A. Taruttis and V. Ntziachristos, "Advances in real-time multispectral optoacoustic imaging and its applications," Nat. Photonics **9**(4), 219–227 (2015).

12. M. Xu and L. V. Wang, "Photoacoustic imaging in biomedicine," Rev. Sci. Instrum. **77**(4), 41101 (2006).

13. K. S. Valluru, B. K. Chinni, N. A. Rao, S. Bhatt, and V. S. Dogra, "Basics and clinical applications of photoacoustic imaging," Ultrasound Clin. **4**(3), 403–429 (2009).

14. S. Zackrisson, S. M. W. Y. van de Ven, and S. S. Gambhir, "Light in and sound out: emerging translational strategies for photoacoustic imaging," Cancer Res. **74**(4), 979–1004 (2014).

15. R. Li, E. Phillips, P. Wang, C. J. Goergen, and J. X. Cheng, "Label-free in vivo imaging of peripheral nerve by multispectral photoacoustic tomography," J. Biophotonics **9**(1-2), 124–128 (2016).

16. L. Nie, X. Cai, K. Maslov, A. Garcia-Uribe, M. A. Anastasio, and L. V. Wang, "Photoacoustic tomography through a whole adult human skull with a photon recycler," J. Biomed. Opt. **17**(11), 110506 (2012).

17. Y.-H. Liu, Y. Xu, L.-D. Liao, K. C. Chan, and N. V. Thakor, "A handheld real-time photoacoustic imaging system for animal neurological disease models: from simulation to realization," Sensors (Basel) **18**(11), 4081 (2018).

18. C. B. Sussman, C. Rossignol, Q. Zhang, H. Jiang, T. Zheng, D. Steindler, L. Young, and M. D. Weiss, "Photoacoustic tomography can detect cerebral hemodynamic alterations in a neonatal rodent model of hypoxia-ischemia," Acta Neurobiol. Exp. (Warsz.) **72**(3), 253–263 (2012).

19. M. Heijblom, D. Piras, M. Brinkhuis, J. C. G. van Hespen, F. M. van den Engh, M. van der Schaaf, J. M. Klaase, T. G. van Leeuwen, W. Steenbergen, and S. Manohar, "Photoacoustic image patterns of breast carcinoma and comparisons with Magnetic Resonance Imaging and vascular stained histopathology," Sci. Rep. **5**(1), 11778 (2015).

20. R. Li, P. Wang, L. Lan, F. P. Lloyd, Jr., C. J. Goergen, S. Chen, and J.-X. Cheng, "Assessing breast tumor margin by multispectral photoacoustic tomography," Biomed. Opt. Express **6**(4), 1273–1281 (2015).

21. L. Xi, S. R. Grobmyer, L. Wu, R. Chen, G. Zhou, L. G. Gutwein, J. Sun, W. Liao, Q. Zhou, H. Xie, and H. Jiang, "Evaluation of breast tumor margins in vivo with intraoperative photoacoustic imaging," Opt. Express **20**(8), 8726–8731 (2012).

22. S. Manohar, S. E. Vaartjes, J. C. G. van Hespen, J. M. Klaase, F. M. van den Engh, W. Steenbergen, and T. G. van Leeuwen, "Initial results of in vivo non-invasive cancer imaging in the human breast using near-infrared photoacoustics," Opt. Express **15**(19), 12277–12285 (2007).

23. R. A. Kruger, R. B. Lam, D. R. Reinecke, S. P. Del Rio, and R. P. Doyle, "Photoacoustic angiography of the breast," Med. Phys. **37**(11), 6096–6100 (2010).

24. Y. Qu, C. Li, J. Shi, R. Chen, S. Xu, H. Rafsanjani, K. Maslov, H. Krigman, L. Garvey, P. Hu, P. Zhao, K. Meyers, E. Diveley, S. Pizzella, L. Muench, N. Punyamurthy, N. Goldstein, O. Onwumere, M. Alisio, K. Meyenburg, J. Maynard, K. Helm, J. Slaughter, S. Barber, T. Burger, C. Kramer, J. Chubiz, M. Anderson, R. McCarthy, S. K. England, G. A. Macones, Q. Zhou, K. K. Shung, J. Zou, M. J. Stout, M. Tuuli, and L. V. Wang, "Transvaginal fast-scanning optical-resolution photoacoustic endoscopy," J. Biomed. Opt. **23**(12), 1–4 (2018).

25. S. Nandy, A. Mostafa, I. S. Hagemann, M. A. Powell, E. Amidi, K. Robinson, D. G. Mutch, C. Siegel, and Q. Zhu, "Evaluation of ovarian cancer: initial application of coregistered photoacoustic tomography and US," Radiology **289**(3), 740–747 (2018).

26. S. E. Bohndiek, L. S. Sasportas, S. Machtaler, J. V. Jokerst, S. Hori, and S. S. Gambhir, "Photoacoustic tomography detects early vessel regression and normalization during ovarian tumor response to the antiangiogenic therapy trebananib," J. Nucl. Med. **56**(12), 1942–1947 (2015).

27. X. Leng, W. Chapman, Jr., B. Rao, S. Nandy, R. Chen, R. Rais, I. Gonzalez, Q. Zhou, D. Chatterjee, M. Mutch, and Q. Zhu, "Feasibility of co-registered ultrasound and acoustic-resolution photoacoustic imaging of human colorectal cancer," Biomed. Opt. Express **9**(11), 5159–5172 (2018).

28. F. Knieling, C. Neufert, A. Hartmann, J. Claussen, A. Urich, C. Egger, M. Vetter, S. Fischer, L. Pfeifer, A. Hagel, C. Kielisch, R. S. Görtz, D. Wildner, M. Engel, J. Röther, W. Uter, J. Siebler, R. Atreya, W. Rascher, D. Strobel, M. F. Neurath, and M. J. Waldner, "Multispectral optoacoustic tomography for assessment of crohn's disease activity," N. Engl. J. Med. **376**(13), 1292–1294 (2017).

29. Y. Cao, J. Hui, A. Kole, P. Wang, Q. Yu, W. Chen, M. Sturek, and J.-X. Cheng, "High-sensitivity intravascular photoacoustic imaging of lipid-laden plaque with a collinear catheter design," Sci. Rep. **6**(1), 25236 (2016).

30. J. Hui, R. Li, P. Wang, E. Phillips, R. Bruning, C.-S. Liao, M. Sturek, C. J. Goergen, and J.-X. Cheng, "Assessing carotid atherosclerosis by fiber-optic multispectral photoacoustic tomography," Proc. SPIE **9323**, 93233S (2015).

31. T. J. Allen, A. Hall, A. P. Dhillon, J. S. Owen, and P. C. Beard, "Spectroscopic photoacoustic imaging of lipid-

rich plaques in the human aorta in the 740 to 1400 nm wavelength range," J. Biomed. Opt. **17**(6), 061209 (2012).

32. D. Razansky, N. J. Harlaar, J. L. Hillebrands, A. Taruttis, E. Herzog, C. J. Zeebregts, G. M. van Dam, and V. Ntziachristos, "Multispectral optoacoustic tomography of matrix metalloproteinase activity in vulnerable human carotid plaques," Mol. Imaging Biol. **14**(3), 277–285 (2012).
33. I. M. Graf, S. Kim, B. Wang, R. Smalling, and S. Emelianov, "Noninvasive detection of intimal xanthoma using combined ultrasound, strain rate and photoacoustic imaging," Ultrasonics **52**(3), 435–441 (2012).
34. B. L. Bungart, L. Lan, P. Wang, R. Li, M. O. Koch, L. Cheng, T. A. Masterson, M. Dundar, and J. X. Cheng, "Photoacoustic tomography of intact human prostates and vascular texture analysis identify prostate cancer biopsy targets," Photoacoustics **11**, 46–55 (2018).
35. S. Sinha, N. A. Rao, B. K. Chinni, and V. S. Dogra, "Evaluation of frequency domain analysis of a multiwavelength photoacoustic signal for differentiating malignant from benign and normal prostates: ex vivo study with human prostates," J. Ultrasound Med. **35**(10), 2165–2177 (2016).
36. R. E. Kumon, C. X. Deng, and X. Wang, "Frequency-domain analysis of photoacoustic imaging data from prostate adenocarcinoma tumors in a murine model," Ultrasound Med. Biol. **37**(5), 834–839 (2011).
37. M. Ai, T. Salcudean, R. Rohling, P. Abolmaesumi, and S. Tang, "Transurethral illumination probe design for deep photoacoustic imaging of prostate," in *Proceedings of SPIE* (SPIE, 2018), Vol. 10494, p. 104940C.
38. H. K. Zhang, Y. Chen, J. Kang, A. Lisok, I. Minn, M. G. Pomper, and E. M. Boctor, "Prostate-specific membrane antigen-targeted photoacoustic imaging of prostate cancer in vivo," J. Biophotonics **11**(9), e201800021 (2018).
39. J. L. Su, R. R. Bouchard, A. B. Karpiouk, J. D. Hazle, and S. Y. Emelianov, "Photoacoustic imaging of prostate brachytherapy seeds," Biomed. Opt. Express **2**(8), 2243–2254 (2011).
40. X. Wang, W. W. Roberts, P. L. Carson, D. P. Wood, and J. B. Fowlkes, "Photoacoustic tomography: a potential new tool for prostate cancer," Biomed. Opt. Express **1**(4), 1117–1126 (2010).
41. S. Huang, Y. Qin, Y. Chen, J. Pan, C. Xu, D. Wu, W. Y. Chao, J. T. Wei, S. A. Tomlins, X. Wang, J. B. Fowlkes, P. L. Carson, Q. Cheng, and G. Xu, "Interstitial assessment of aggressive prostate cancer by physio-chemical photoacoustics: An ex vivo study with intact human prostates," Med. Phys. **45**(9), 4125–4132 (2018).
42. A. Horiguchi, K. Tsujita, K. Irisawa, T. Kasamatsu, K. Hirota, M. Kawaguchi, M. Shinchi, K. Ito, T. Asano, H. Shinmoto, H. Tsuda, and M. Ishihara, "A pilot study of photoacoustic imaging system for improved real-time visualization of neurovascular bundle during radical prostatectomy," Prostate **76**(3), 307–315 (2016).
43. A. Horiguchi, M. Shinchi, A. Nakamura, T. Wada, K. Ito, T. Asano, H. Shinmoto, H. Tsuda, and M. Ishihara, "Pilot study of prostate cancer angiogenesis imaging using a photoacoustic imaging system," Urology **108**, 212–219 (2017).
44. Z. Xie, W. Roberts, P. Carson, X. Liu, C. Tao, and X. Wang, "Evaluation of bladder microvasculature with high-resolution photoacoustic imaging," Opt. Lett. **36**(24), 4815–4817 (2011).
45. A. Kamaya, S. Vaithilingam, B. I. Chung, O. Oralkan, and B. T. Khuri-Yakub, "Photoacoustic imaging of the bladder: a pilot study," J. Ultrasound Med. **32**(7), 1245–1250 (2013).
46. C. Kim, M. Jeon, and L. V. Wang, "Nonionizing photoacoustic cystography in vivo," Opt. Lett. **36**(18), 3599–3601 (2011).
47. K. Sivasubramanian, V. Periyasamy, R. A. Dienzo, and M. Pramanik, "Hand-held, clinical dual mode ultrasound - photoacoustic imaging of rat urinary bladder and its applications," J. Biophotonics **11**(5), e201700317 (2018).
48. O. Ogunlade, J. J. Connell, J. L. Huang, E. Zhang, M. F. Lythgoe, D. A. Long, and P. Beard, "In vivo three-dimensional photoacoustic imaging of the renal vasculature in preclinical rodent models," Am. J. Physiol. Renal Physiol. **314**(6), F1145–F1153 (2018).
49. K. Okumura, J. Matsumoto, Y. Iwata, K. Yoshida, N. Yoneda, T. Ogi, A. Kitao, K. Kozaka, W. Koda, S. Kobayashi, D. Inoue, N. Sakai, K. Furuichi, T. Wada, and T. Gabata, "Evaluation of renal oxygen saturation using photoacoustic imaging for the early prediction of chronic renal function in a model of ischemia-induced acute kidney injury," PLoS One **13**(12), e0206461 (2018).
50. E. S. L. Berndl, X. He, D. A. Yuen, and M. C. Kolios, "Photoacoustic imaging for assessing ischemic kidney damage in vivo," in *Proceedings of SPIE* (2018), Vol. 10494, p. 104941P–10494–7.
51. A. Shah, T. Delgado-Goni, T. Casals Galobart, S. Wantuch, Y. Jamin, M. O. Leach, S. P. Robinson, J. Bamber, and M. Beloueche-Babari, "Detecting human melanoma cell re-differentiation following BRAF or heat shock protein 90 inhibition using photoacoustic and magnetic resonance imaging," Sci. Rep. **7**(1), 8215 (2017).
52. R. M. Weight, J. A. Viator, P. S. Dale, C. W. Caldwell, and A. E. Lisle, "Photoacoustic detection of metastatic melanoma cells in the human circulatory system," Opt. Lett. **31**(20), 2998–3000 (2006).
53. Y. Wang, D. Xu, S. Yang, and D. Xing, "Toward in vivo biopsy of melanoma based on photoacoustic and ultrasound dual imaging with an integrated detector," Biomed. Opt. Express **7**(2), 279–286 (2016).
54. Y. Zhou, W. Xing, K. I. Maslov, L. A. Cornelius, and L. V. Wang, "Handheld photoacoustic microscopy to detect melanoma depth in vivo," Opt. Lett. **39**(16), 4731–4734 (2014).
55. X. Li, D. Wang, H. Ran, L. Hao, Y. Cao, M. Ao, N. Zhang, J. Song, L. Zhang, H. Yi, Z. Wang, and P. Li, "A preliminary study of photoacoustic/ultrasound dual-mode imaging in melanoma using MAGE-targeted gold nanoparticles," Biochem. Biophys. Res. Commun. **502**(2), 255–261 (2018).
56. P. J. van den Berg, R. Bansal, K. Daoudi, W. Steenbergen, and J. Prakash, "Preclinical detection of liver fibrosis using dual-modality photoacoustic/ultrasound system," Biomed. Opt. Express **7**(12), 5081–5091 (2016).
57. Y. Zhu, L. A. Johnson, Z. Huang, J. M. Rubin, J. Yuan, H. Lei, J. Ni, X. Wang, P. D. R. Higgins, and G. Xu, "Identifying intestinal fibrosis and inflammation by spectroscopic photoacoustic imaging: an animal study *in*

vivo," Biomed. Opt. Express **9**(4), 1590–1600 (2018).

58. G. Russo, M. Mischi, W. Scheepens, J. J. De la Rosette, and H. Wijkstra, "Angiogenesis in prostate cancer: onset, progression and imaging," BJU Int. **110**(11 Pt C 11 Pt C), E794–E808 (2012).

59. S. Yue, J. Li, S.-Y. Lee, H. J. Lee, T. Shao, B. Song, L. Cheng, T. A. Masterson, X. Liu, T. L. Ratliff, and J.-X. Cheng, "Cholesteryl ester accumulation induced by PTEN loss and PI3K/AKT activation underlies human prostate cancer aggressiveness," Cell Metab. **19**(3), 393–406 (2014).

60. S. Tang, J. Chen, P. Samant, K. Stratton, and L. Xiang, "Transurethral photoacoustic endoscopy for prostate cancer: a simulation study," IEEE Trans. Med. Imaging **35**(7), 1780–1787 (2016).

61. M. A. Lediju Bell, X. Guo, D. Y. Song, and E. M. Boctor, "Transurethral light delivery for prostate photoacoustic imaging," J. Biomed. Opt. **20**(3), 036002 (2015).

62. A.-A. Yassine, L. Lilge, and V. Betz, "Optimizing interstitial photodynamic therapy with custom cylindrical diffusers," J. Biophotonics **12**(1), e201800153 (2019).

63. J. C. Mizeret and H. E. van den Bergh, "Cylindrical fiberoptic light diffuser for medical applications," Lasers Surg. Med. **19**(2), 159–167 (1996).

64. M. Li, B. Lan, W. Liu, J. Xia, and J. Yao, "Internal-illumination photoacoustic computed tomography," J. Biomed. Opt. **23**(3), 1–4 (2018).

65. T. H. Nguyen, Y. H. Rhee, J. C. Ahn, and H. W. Kang, "Circumferential irradiation for interstitial coagulation of urethral stricture," Opt. Express **23**(16), 20829–20840 (2015).

66. *ANSI Z136.1 - Safe Use of Lasers* (American National Standards Institute, Inc., 2007).

67. W. H. Nau, R. J. Roselli, and D. F. Milam, "Measurement of thermal effects on the optical properties of prostate tissue at wavelengths of 1,064 and 633 nm," Lasers Surg. Med. **24**(1), 38–47 (1999).

68. A. E. Worthington, J. Trachtenberg, and M. D. Sherar, "Ultrasound properties of human prostate tissue during heating," Ultrasound Med. Biol. **28**(10), 1311–1318 (2002).

69. J. R. Cook, R. R. Bouchard, and S. Y. Emelianov, "Tissue-mimicking phantoms for photoacoustic and ultrasonic imaging," Biomed. Opt. Express **2**(11), 3193–3206 (2011).

70. M. Fonseca, B. Zeqiri, P. C. Beard, and B. T. Cox, "Characterisation of a phantom for multiwavelength quantitative photoacoustic imaging," Phys. Med. Biol. **61**(13), 4950–4973 (2016).

71. D. D. Royston, R. S. Poston, and S. A. Prahl, "Optical properties of scattering and absorbing materials used in the development of optical phantoms at 1064 nm," J. Biomed. Opt. **1**(1), 110–116 (1996).

72. F. Padera, "Measuring absorptance (k) and refractive index (n) of thin films with the perkinelmer lambda 950/1050 high performance UV-Vis/NIR spectrometers," PerkinElmer, Inc. (2013).

73. N. Sultanova, S. Kasarova, and I. Nikolov, "Dispersion properties of optical polymers," in *Proceedings of the International School and Conference on Photonics* (2009), **116**, pp. 585–587.

74. H. J. van Staveren, C. J. M. Moes, J. van Marie, S. A. Prahl, and M. J. C. van Gemert, "Light scattering in Intralipid-10% in the wavelength range of 400-1100 nm," Appl. Opt. **30**(31), 4507–4514 (1991).

75. J. Crisp and B. Elliott, *Introduction to Fiber Optics*, 3rd ed. (Elsevier, 2005).

76. D. Georgescu, E. Alexandrescu, R. Multescu, and B. Geavlete, "Cystoscopy and urinary bladder anatomy," in *Endoscopic Diagnosis and Treatment in Urinary Bladder Pathology* (Elsevier Inc., 2016), pp. 1–24.

77. E. B. Stechel, K. D. Meeks, W. M. Trott, P. E. Klingsporn, and D. M. Berry, "High-power transmission through step-index multimode fibers," Proc. SPIE **1441**, 61–70 (1991).

78. M. Ai, W. Shu, T. Salcudean, R. Rohling, P. Abolmaesumi, and S. Tang, "Design of high energy laser pulse delivery in a multimode fiber for photoacoustic tomography," Opt. Express **25**(15), 17713–17726 (2017).

79. E. B. Stechel, "Laser-induced damage in step-index multimode fibers," Proc. SPIE **1848**, 15–24 (1993).

80. K. Irisawa, T. Hirasawa, K. Hirota, K. Tsujita, and M. Ishihara, "Influence of laser pulse width to the photoacoustic temporal waveform and the image resolution with a solid-state excitation laser," in *Proc. of SPIE, Photons Plus Ultrasound: Imaging and Sensing* (2012), Vol. **8223W**, p. 82232W.

81. H. Moradi, S. Tang, and S. E. Salcudean, "Toward intra-operative prostate photoacoustic imaging: configuration evaluation and implementation using the da Vinci research kit," IEEE Trans. Med. Imaging **38**(1), 57–68 (2019).

82. P.-T. Dong, H. Mohammad, X. Wang, J. Hui, J. Li, L. Liang, M. N. Seleem, and J.-X. Cheng, "Annihilation of methicillin-resistant staphylococcus aureus via photobleaching of staphyloxanthin," bioRxiv, 227603 (2017).